micromachines

MDPI

Article

Effect of High Temperature During Packaging Process on the Dynamic Parameter Stability of Hemispherical Resonator Gyroscope

Ming Kang [1,2], Yao Pan [1,2], Yiming Luo [1,2,*], Kaiyong Yang [1,2,*], Yonglei Jia [1,2], Hui Luo [1,2], Jianhua Shi [1,2], Shihao Zhu [1,2] and Xiaomeng Jia [2]

[1] College of Advanced Interdisciplinary Studies, National University of Defense Technology, Changsha 410073, China; kangming232@163.com (M.K.); yaomeredithpan@hotmail.com (Y.P.); jiayonglei17@nudt.edu.cn (Y.J.); luohui.luo@163.com (H.L.); shijh@nudt.edu.cn (J.S.); zshero2002@163.com (S.Z.)

[2] Nanhu Laser Laboratory, National University of Defense Technology, Changsha 410073, China; jiax1aomeng@sina.com

* Correspondence: luoyiming11@nudt.edu.cn (Y.L.); yky208@nudt.edu.cn (K.Y.); Tel.: +86-193-7488-5727 (Y.L.); +86-137-5511-5175 (K.Y.)

Abstract

During hemispherical resonator gyroscope (HRG) packaging, localized high temperatures cause nonuniform thermal distributions and degrade the stability of key dynamic parameters. To reduce these temperature effects, the HRG thermal field was analyzed using coupled simulations in COMSOL Multiphysics. First, the mechanisms for local high temperatures were analyzed. Second, thermal simulations of getter activation and hermetic welding were performed and optimization strategies were proposed. Third, the effects of housing materials and structural dimensions were investigated to further optimize the temperature effects. Finally, dynamic parameter stability experiments were conducted to evaluate the optimization effectiveness. Compared with the original packaging process, the optimization significantly reduced the disturbance effect of the high temperature on the key dynamic parameters. Throughout packaging, the maximum quality factor (Q factor) reached 1.775×10^7, the frequency split (Δf) remained below 1 mHz and the Q factor inhomogeneity (ΔQ) remained below 3.7%, indicating that the dynamic parameters of the gyroscope were well preserved. Meanwhile, the measured leak rates remained below 1×10^{-12} Pa·m^3/s. These results demonstrate the optimization effectively mitigates packaging-induced thermal disturbances, improving dynamic parameter stability with excellent hermeticity. This provides a reliable dynamic parameter basis for the high-performance operation of the HRG.

Keywords: hemispherical resonator gyroscope; Multiphysics coupling; structure and packaging; temperature field

Check for updates

Academic Editors: Cao Xia, Jie Song and Dongfang Wang

Received: 24 September 2026
Revised: 28 October 2026
Accepted: 29 October 2026
Published: 31 October 2026

Copyright: © 2026 by the authors. Licensee MDPI, Basel, Switzerland. This article is an open access article distributed under the terms and conditions of the Creative Commons Attribution (CC BY) license.

1. Introduction

At present, accurate navigation, positioning, and attitude control technologies have become essential foundational elements across multiple industries. As a high-precision inertial sensor, the hemispherical resonator gyroscope (HRG) plays a pivotal role in aerospace, national defense, geological exploration, intelligent transportation, and numerous other domains [1–3]. Its core principle involves utilizing the standing wave of mechanical vibration to detect external angular velocity, thereby enabling accurate measurement of the motion state.

However, HRG performance is highly sensitive to environmental disturbances, among which temperature is particularly important [4,5]. Temperature variations can induce changes in key gyroscope parameters, including the quality factor (Q factor), frequency split (Δf), and quality factor inhomogeneity (ΔQ) [6]. Even small variations in these parameters may result in additional errors during operation. Consequently, the measurement accuracy and stability of the HRG can be degraded [7,8].

Thermal effects can arise at two distinct stages: during service operation after packaging and during the packaging process. Most previous studies have focused on thermal effects during the operational stage after packaging. Zhao [9] proposed a high-reliability HRG with a constant-temperature control scheme to mitigate the influence of ambient temperature variations. Zeng [10] developed a self-calibration control algorithm based on mode reversal to improve HRG performance under large temperature variations. Xu [11] established a thermoelastic model for a thermally stressed hemispherical shell resonator (TM-HSR) and investigated the effect of thermal deformation on HRG output.

By contrast, thermal effects generated during the packaging process have received much less attention. Two major packaging steps involve intense localized heating: getter activation and cover-plate laser welding. The getter needs to be heated to approximately 800 °C and maintained at this temperature for 20 min, whereas laser welding generates a much higher local temperature around the weld region. Heat produced by these localized sources is transferred to the housing, glass-to-metal seals, and resonator, resulting in nonuniform temperature distributions. Because HRG components have limited temperature tolerance, excessive thermal loading may impair the hermetic sealing structure and alter the thermal state of the resonator. The extremely low leakage rate and optimal dynamic-parameter stability during the packaging process of HRGs may therefore be affected. These packaging-induced thermal effects require further investigation and targeted optimization. In addition to the packaging conditions, the thermal response of the HRG is also affected by its material properties and structural dimensions, which determine the heat-transfer paths and temperature distribution. Therefore, the packaging process, material selection, and structural parameters should be optimized in a coordinated manner.

In this work, the thermal behavior of the HRG during getter activation and laser welding was systematically investigated. COMSOL Multiphysics 6.2 simulations were performed to evaluate the temperature field and identify thermal risks during packaging. The getter activation strategy, housing material, structural dimensions, and laser welding parameters were subsequently optimized. The effects of different materials and dimensions on the HRG temperature field were also investigated to guide structural design. Finally, the optimized HRGs were experimentally evaluated in terms of hermeticity and dynamic parameter stability. Leak rates below 1×10^{-12} Pa·m^3/s, Δf values below 1 mHz, a maximum Q factor of 1.775×10^7, and ΔQ values below 3.7% were obtained. These results confirm that the proposed optimization effectively suppresses packaging-induced thermal effects while preserving the hermeticity and dynamic parameter stability of the HRG.

2. Theoretical Analysis of Thermal Simulation for the HRG

2.1. Structural Overview of the HRG

At present, the HRG typically adopts a two-piece structure, which is primarily composed of a resonator and an electrode plate. Both components are fabricated from fused silica. They are subjected to processes such as annealing, cleaning, leveling, and metallization to form the resonator assembly. Subsequently, the resonator assembly is encapsulated in a metal housing, resulting in the HRG structure. The external structural layout of the HRG is illustrated in Figure 1a.

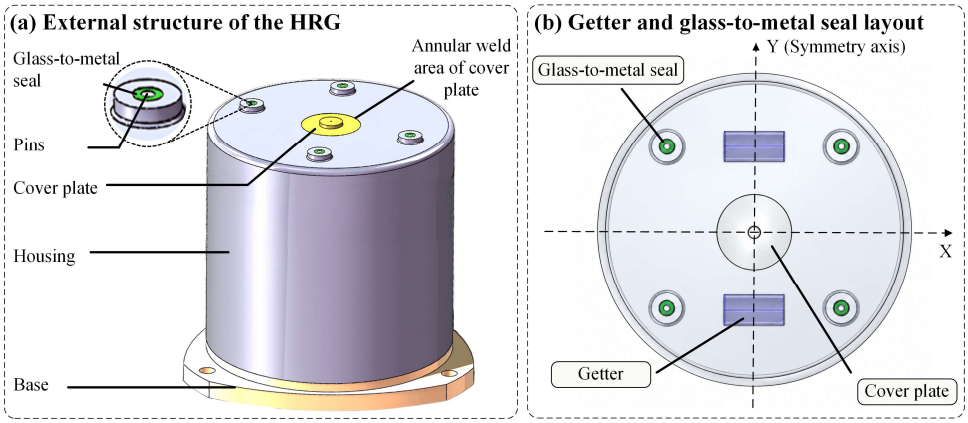

Figure 1. HRG package structure and thermal-source layout: (**a**) external structure of the HRG; (**b**) relative positions of the getters and glass-to-metal seals.

The HRG package forms a sealed cavity that provides the high-vacuum environment required for resonator operation. Such a vacuum reduces resonator energy dissipation and helps maintain a high Q factor [12,13]. The HRG cavity is first evacuated through the central pumping port. Residual gases are subsequently adsorbed by two non-evaporable getters to maintain the vacuum during operation. As shown in Figure 1b, the two getters are arranged symmetrically inside the package and are electrically connected to the nearby pins. This configuration also establishes the main heat-transfer paths from the getters to the glass-to-metal seals during electrical activation.

Getter activation constitutes the first major thermal-risk condition during packaging. In the present process, the getter is heated to approximately 800 °C and maintained at this temperature for 20 min. For the engineering evaluation in this work, 200 °C was adopted as the temperature tolerance for the glass-to-metal seals according to the packaging-process criterion used in the experiment. Because the getter is electrically connected to the nearby seals through the pins, heat generated during activation can be transferred to the seals by solid conduction along the pins and by thermal radiation across the evacuated cavity. Consequently, the regions near the pin–seal interfaces are particularly susceptible to localized overheating. Temperatures exceeding the adopted limit may increase the risk of degradation of the sealing structure and, consequently, impair package hermeticity. The 200 °C limit was specified by the glass-to-metal seal manufacturer for the sealing material used in this assembly and was adopted as the engineering temperature criterion.

Cover plate laser welding constitutes the second major thermal-risk condition. Both the cover plate and housing are made of Kovar alloy. During circumferential welding, the annular weld region must reach at least the melting temperature of the alloy, approximately 1450 °C. The generated heat is conducted radially through the cover plate toward the peripheral glass-to-metal seals. Excessive heat accumulation may therefore cause local seal temperatures to exceed their allowable range.

Accordingly, getter activation and cover plate laser welding are treated as the two principal heat-source conditions in this work. Their thermal effects on the glass-to-metal seals and other temperature-sensitive HRG components are evaluated using the coupled thermal model described in the following subsection.

2.2. Thermodynamic Simulation Analysis

During the thermal simulation in this work, the Heat Transfer in Solids interface and Surface-to-Surface Radiation interface in COMSOL Multiphysics® (License No. 9420394) were used. The Heat Transfer in Solids interface was employed to simulate heat transfer through the motion of molecules and atoms within the HRG components. Meanwhile, the

Surface-to-Surface Radiation interface was used to model thermal radiation between the internal surfaces of the HRG. Since the simulation was conducted in a vacuum environment, convective heat transfer, which relies on gas as the medium, could be neglected [14].

During the processes of getter activation and cover plate welding, the governing equation for the Heat Transfer in Solids interface is as follows:

$$\rho C \frac{\partial T}{\partial t} + \nabla \cdot (-k \nabla T) = S \tag{1}$$

where ρ is the density, C is the specific heat capacity, T is the temperature, k is the thermal conductivity, and S is the heat source term. In the simulation of this study, the heat sources corresponding to S are the getter and the annular welding area of the cover plate. The getter is represented by its prescribed activation-temperature history, whereas the laser is represented by the moving Gaussian boundary heat flux described in Section 4. The 60 °C housing condition is used only for the active-cooling cases.

The governing equation for the Surface-to-Surface Radiation interface is as follows:

$$J = \varepsilon e_b(T) + \rho_d G \tag{2}$$

$$G \equiv G_m + G_{amb} + G_{ext} \tag{3}$$

$$e_b(T) = n^2 \sigma T^4 \tag{4}$$

where J is the total surface radiative heat flux, ε is the surface emissivity of the material, $e_b(T)$ is the blackbody radiant power density, ρ_d is the diffuse reflectivity, G is the total incident radiation, n is the refractive index, σ is the Stefan-Boltzmann constant, G_m is the incident radiation from other surfaces, G_{amb} is the ambient radiation, and G_{ext} is the external radiation.

In this work, only the mutual radiation between the various surfaces inside the HRG cavity was considered. Therefore, both G_{amb} and G_{ext} were assumed to be 0, leading to $G = G_m$.

3. Thermal Simulation of the Getter Activation Process

The non-evaporable getters used in HRGs are generally based on zirconium or titanium with appropriate amounts of other metals added. They are either fabricated into an alloy through smelting or formed by sintering mixed powders [15–17]. Prior to being put into service, such non-evaporable getters must be subjected to heating activation in a vacuum environment. This step is primarily intended to remove the passivation layer on their surface and expose the internal clean metal layer, thereby enabling them to achieve gas absorption capability and complete the activation process [18].

Due to the inherent electrical conductivity of the getter alloy, the electrical heating method can be adopted to activate it. During the getter activation process, changes in the temperature distribution are mainly affected by the heat source. The temperature and heating duration of the heat source are key parameters [19]. Different getters have different activation temperatures, but all require a high temperature to be maintained for a certain period [20].

In the present process, the getter was electrically heated to 800 °C and maintained for 20 min. This high activation temperature may cause local overheating of the glass-to-metal seals and compromise package hermeticity.

As shown in Figure 1b, two getters are arranged symmetrically inside the HRG package. Accordingly, two activation modes were considered. In single-getter activation, only one getter is energized at a time, whereas in dual-getter activation, both getters are activated simultaneously. Single-getter activation reduces the instantaneous thermal load introduced by the heat sources, but the asymmetric heating may produce a nonuniform temperature field in the resonator. By contrast, simultaneous dual-getter activation provides a more

symmetric heat input and shortens the overall activation process, although the resulting thermal load on the glass-to-metal seals must be evaluated. Therefore, the thermal responses under these two activation modes were compared by simulation.

3.1. Single-Getter Activation

For the single-getter case, only the lower getter in Figure 2a was activated. In the simulation, the getter temperature was increased linearly from 20 °C to 800 °C within 1 min and was then maintained at 800 °C for 20 min. The two glass-to-metal seals adjacent to the active getter and directly connected to it through the pins were defined as Group B, whereas the two seals on the opposite side were defined as Group A.

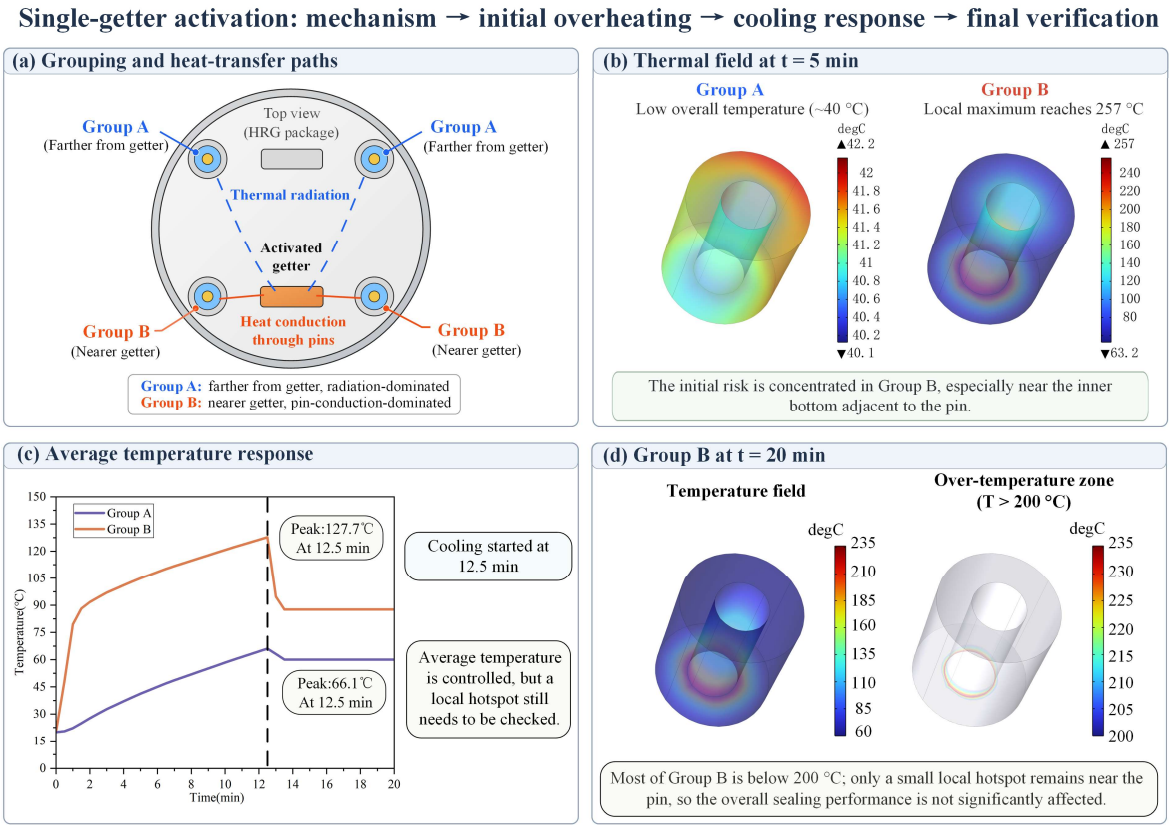

Figure 2. Single-getter activation: (**a**) seal grouping and dominant heat-transfer paths; (**b**) seal temperature fields at t = 5 min; (**c**) average seal-temperature response with event-triggered cooling; (**d**) Group B temperature field and T > 200 °C region at t = 20 min.

Figure 2a illustrates the seal grouping and the dominant heat-transfer paths during single-getter activation. For Group A, no direct conductive path exists between the active getter and the seals, and heating is therefore dominated by thermal radiation. In contrast, Group B is directly connected to the active getter through the pins, making heat conduction the dominant heat-transfer mechanism.

The seal temperature fields after 5 min of activation are shown in Figure 2b. The two groups exhibit distinctly different temperature distributions, consistent with their respective heat-transfer mechanisms. For Group A, the overall temperature remains only slightly above 40 °C because of the relatively weak radiative heating. The warmer region is mainly concentrated on the cylindrical surface facing the active getter, where the incident thermal radiation is strongest. For Group B, heat is conducted directly through the pin, and the high-temperature region is therefore concentrated near the inner portion of the seal adjacent to the pin. A local maximum of approximately 257 °C is reached in this region,

exceeding the 200 °C temperature tolerance of the glass-to-metal seal. This result indicates that local overheating can occur within 5 min of single-getter activation.

To mitigate this overheating, the housing-surface temperature was monitored during getter activation. At approximately $t = 12.5$ min, the housing temperature reached 60 °C. From this time onward, a constant-temperature boundary condition of 60 °C was applied to the housing to represent the cooling procedure used in engineering practice and to maintain the housing temperature at approximately 60 °C.

As shown in Figure 2c, after the cooling condition is applied at approximately $t = 12.5$ min, the average temperatures of both Group A and Group B decrease rapidly and subsequently stabilize well below 200 °C. However, the average seal temperature cannot fully characterize the risk of localized overheating, particularly for Group B, where heat is concentrated near the pin. Therefore, the local temperature field of Group B was further examined after thermal stabilization.

Figure 2d shows the temperature field of the Group B seal at $t = 20$ min. Most of the seal remains below 200 °C, while only a small region near the pin exceeds the temperature tolerance. These results indicate that active cooling substantially reduces the thermal load and confines the over-temperature region to a small localized area. The small predicted region above 200 °C indicates a localized risk rather than demonstrating seal failure. Practical hermeticity was evaluated after packaging.

3.2. Dual-Getter Activation

Although cooling confines the over-temperature region during single-getter activation to a small localized area, it still exhibits certain limitations. Compared with the simultaneous heating of dual getters, single-getter activation results in a nonuniform temperature field in the resonator. The resonator beneath the getter is a temperature-sensitive device [21]. Thus, the nonuniform temperature field will affect the stability of the resonator's physical performance parameters. To improve the thermal symmetry of the resonator while maintaining the thermal safety of the glass-to-metal seals, simultaneous dual-getter activation was further investigated. Figure 3 summarizes the dual-getter activation configuration and its thermal response, including the heat-transfer paths, resonator temperature distribution, seal-temperature evolution, and local over-temperature regions.

As shown in Figure 3a, the two getters are activated simultaneously and are symmetrically arranged on opposite sides of the package. Each getter is directly connected to the two nearby glass-to-metal seals through the corresponding pins. Heat is therefore transferred mainly from each getter to the same-side seals by conduction through the pins, while thermal radiation from the opposite getter provides an additional but weaker heat-transfer path. Owing to the symmetric arrangement of the two heat sources, the four glass-to-metal seals exhibit equivalent thermal conditions during dual-getter activation. Therefore, one representative seal was selected for subsequent quantitative analysis.

Figure 3b compares the resonator temperature fields under single-getter and dual-getter activation. In the single-getter case, the high-temperature region is concentrated on one side of the resonator, and the temperature centroid deviates from the geometric center. In contrast, simultaneous dual-getter activation produces a substantially more symmetric temperature distribution, with the temperature centroid located closer to the geometric center. This improved thermal symmetry is expected to reduce asymmetric thermal stress and the associated variation in frequency split. A nonuniform temperature field produces differential thermal strain, which can generate asymmetric stress and perturb the modal stiffness and frequency split when deformation is constrained [11]. This physical interpretation is not a substitute for a separate thermal-structural calculation.

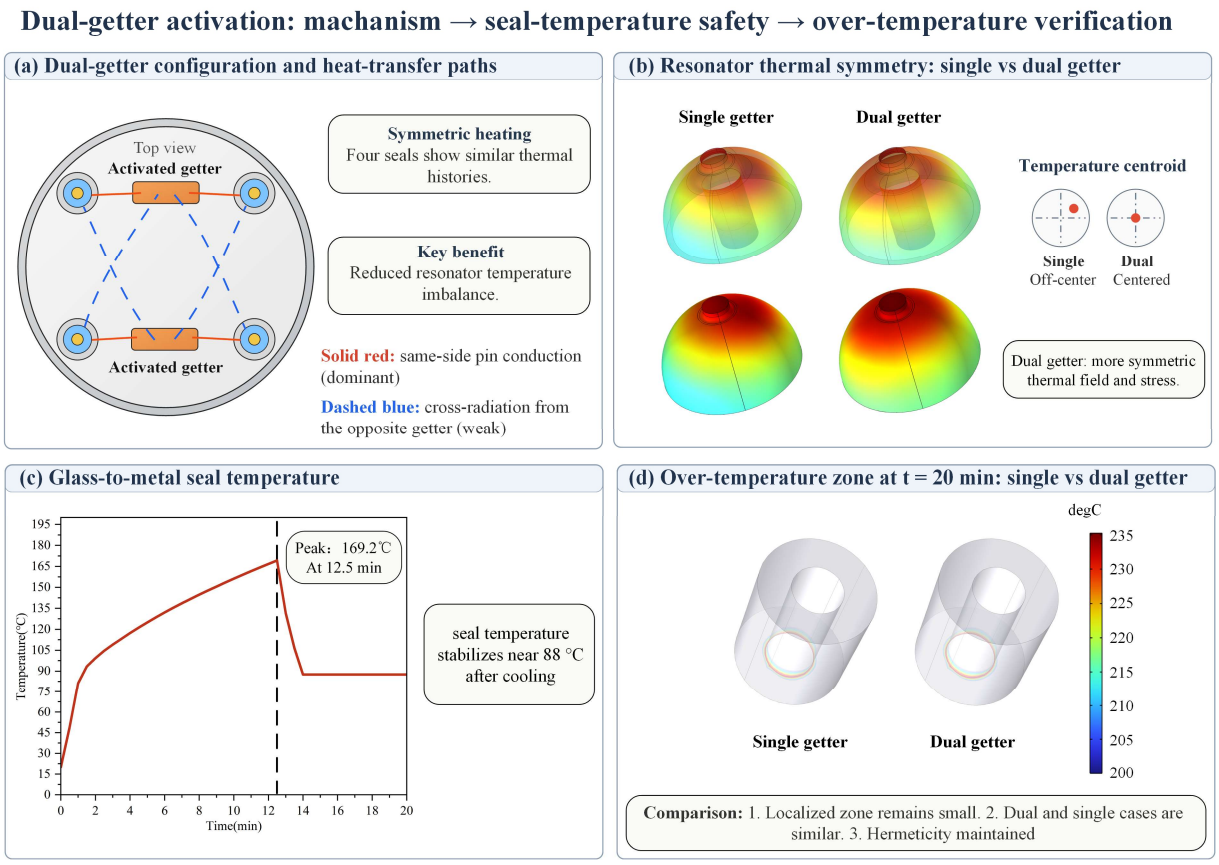

Figure 3. Dual-getter activation: (**a**) symmetric getter configuration and heat-transfer paths; (**b**) resonator thermal symmetry for single-getter and dual-getter activation; (**c**) representative seal-temperature response; (**d**) comparison of the $T > 200$ °C regions at $t = 20$ min.

The average temperature response of a representative glass-to-metal seal is shown in Figure 3c. The temperature increases to a peak of approximately 169.2 °C at $t = 12.5$ min and then decreases to about 88 °C after cooling is activated. The overall response is similar to that of Group B under single-getter activation. This similarity indicates that heat conduction from the same-side getter through the pins remains the dominant heat-transfer mechanism, whereas thermal radiation from the opposite getter has a relatively small contribution.

Although the average seal temperature remains below the 200 °C tolerance, a local hot spot may still exist near the pin. Therefore, the local over-temperature regions were further examined. As shown in Figure 3d, the $T > 200$ °C region at $t = 20$ min remains small and is comparable to that observed during single-getter activation. This result indicates that activating the second getter does not materially enlarge the critical local overheating region of the glass-to-metal seals.

Taken together, simultaneous dual-getter activation improves the thermal symmetry of the resonator without significantly increasing the thermal risk of the glass-to-metal seals. It also shortens the overall activation process compared with sequential single-getter activation.

4. Thermal Simulation of the Welding Process

During the packaging process of the HRG, maintaining a vacuum environment is one of the key factors to ensure its performance. Therefore, before the gyroscope is connected to a vacuum pumping station, hermetic packaging of the structure needs to be realized through laser welding. This process specifically involves two steps. The first is welding the seam between the housing and the base, and the second is welding the annular welding area

of the cover plate (as shown in Figure 1a). Since the first step is far from the glass-to-metal seal area, there are few thermally induced failure factors during the welding process. No hermeticity failure occurred during welding at this position in the actual production process. It was not the focus of this work, and only the second welding step was analyzed.

The welding of the cover plate is achieved via laser circumferential welding. In the COMSOL simulations conducted herein, welding simulations of the circumferential cover plate region are performed by specifying the corresponding laser welding parameters. The laser heat input during cover-plate welding was implemented using the Boundary Heat Source feature in the Heat Transfer in Solids interface. On the welding surface, the prescribed boundary condition is:

$$-n \cdot q = Q_b \tag{5}$$

where n is the outward unit normal vector, q is the conductive heat-flux vector, and Q_b is the applied boundary heat source. In the present model, Q_b was specified by a user-defined function $H(x, z, t)$ to represent the spatial Gaussian distribution and circumferential motion of the laser beam:

$$Q_b = H(x,z,t) = \frac{\lambda P}{\pi r_s^2} exp\left(-\frac{(x - x_0 - Rcos(\omega t))^2 + (z - z_0 - Rsin(\omega t))^2}{r_s^2} \right) \tag{6}$$

where H is heat flux density, λ is laser thermal efficiency, P is laser power, r_s is laser spot radius, R is the radius of circular scanning path, ω is angular scanning velocity, x_0 and z_0 are coordinate of scan center in x and z directions. In the present simulations, the key parameters are specified as follows: $\lambda = 0.8$, $P = 1000$ W, $r_s = 0.75$ mm, $R = 0.5$ mm, and $\omega = 0.65$ rad/s.

Given the inherently short duration of laser welding, the total simulation duration is set to 10 s with a time step of 0.01 s, which enables the observation of temperature evolution in the glass-metal hermetic seal structure. Furthermore, the welding process is characterized by its short duration and extremely steep instantaneous temperature gradients. Consequently, no constant-temperature boundary conditions were imposed in the simulation. Figure 4 illustrates the laser welding process and the corresponding temperature evolution across the cross-section of the cover plate.

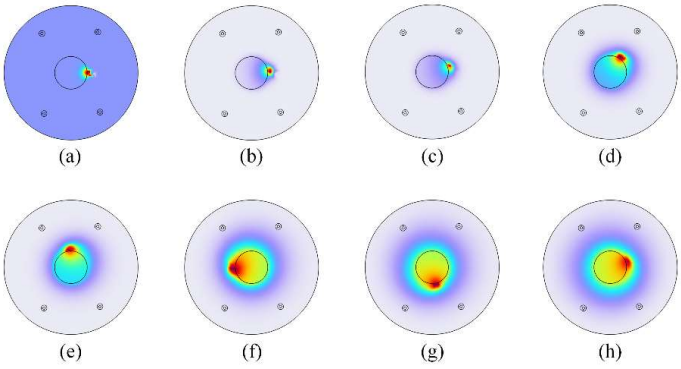

Figure 4. Temperature change diagrams of the cross-section of the gyroscope cover. (**a**) $t = 0.01$ s; (**b**) $t = 0.25$ s; (**c**) $t = 0.5$ s; (**d**) $t = 1.5$ s; (**e**) $t = 2.5$ s; (**f**) $t = 5$ s; (**g**) $t = 7.5$ s; (**h**) $t = 10$ s.

As shown in Figure 4, at the beginning of welding, the high-temperature region is confined to the annular weld area, while the peripheral glass-to-metal seals remain close to room temperature. As welding proceeds, heat gradually diffuses outward through the cover plate. After approximately 2.5 s, the thermal front begins to extend toward the peripheral seals. By 5 s, the seals start to experience a noticeable temperature rise, and further welding causes the thermal load on the seals to increase continuously. These results

indicate that prolonged welding allows the heat generated at the annular weld to propagate to the glass-to-metal seals.

However, the temperature distribution within each glass-to-metal seal is highly nonuniform because the heat reaches the seal predominantly from the side facing the annular weld. Therefore, the overall average seal temperature alone cannot accurately characterize the local overheating risk. To clarify the heat-transfer mechanism and identify the region most susceptible to overheating, the heat-transfer path and the corresponding radial division of the seal are illustrated in Figure 5.

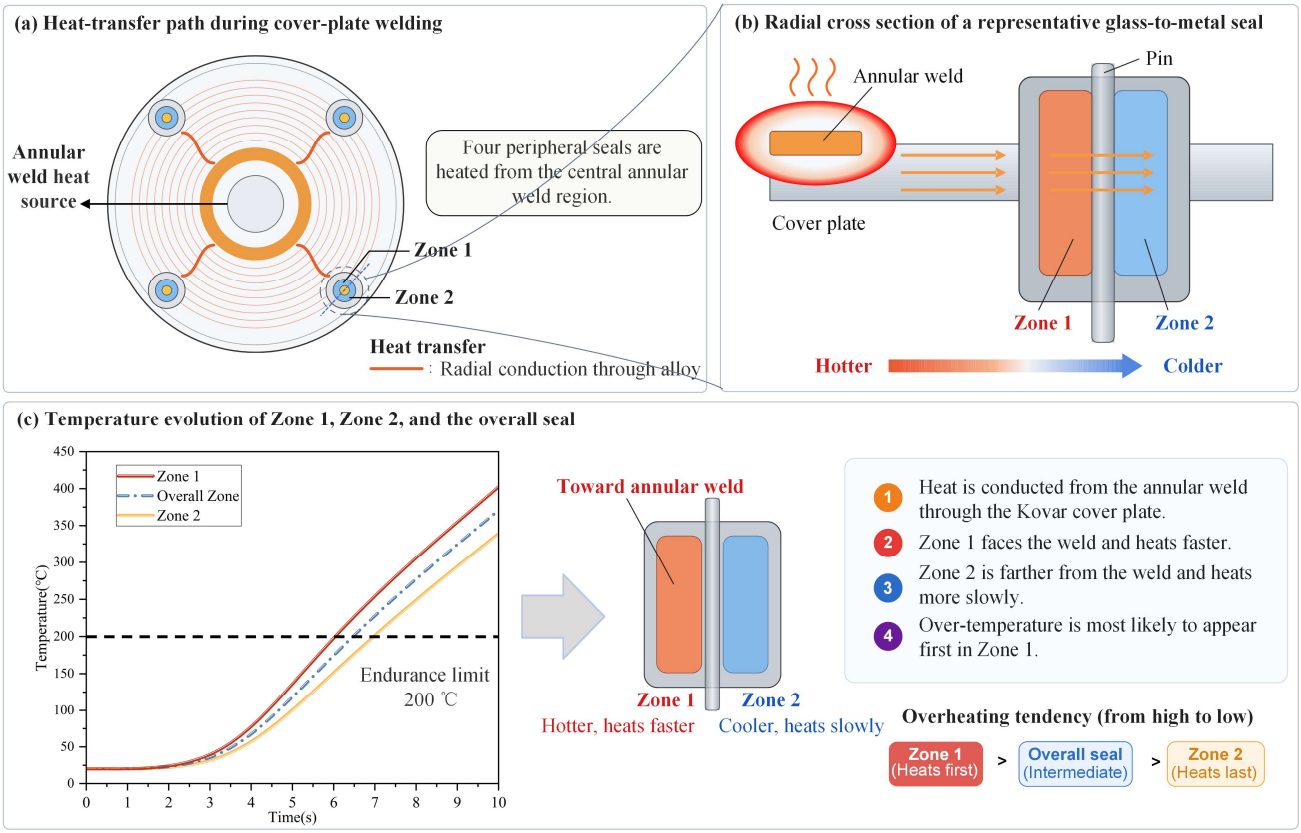

Figure 5. Heat-transfer mechanism and nonuniform temperature response of a representative glass-to-metal seal during cover-plate welding: (**a**) radial heat-transfer path; (**b**) radial cross section and definition of Zone 1 and Zone 2; (**c**) temperature histories and overheating tendency.

As shown in Figure 5a, heat generated at the annular weld is conducted radially outward through the Kovar cover plate toward the four peripheral glass-to-metal seals. Based on this heat-flow direction, the seal cross section is divided into two regions in Figure 5b. Zone 1 is the half facing the annular weld, whereas Zone 2 is the opposite half farther from the weld. Because Zone 1 receives the conducted heat first, its temperature rises faster than that of Zone 2. Local overheating is therefore expected to initiate in Zone 1.

The temperature histories of Zone 1, Zone 2, and the overall seal are compared in Figure 5c. During the first approximately 2 s, the temperatures of all three regions remain close to room temperature. They then increase rapidly as heat propagates outward from the weld. At t = 10 s, the average temperatures of Zone 1, the overall seal, and Zone 2 reach approximately 400, 370, and 340 °C, respectively. All three values exceed the 200 °C temperature tolerance of the glass-to-metal seal, with Zone 1 exhibiting the highest temperature. In particular, the average temperature of Zone 1 approaches 200 °C at approximately 6 s, indicating that the weld-facing side becomes thermally critical first.

To further determine the onset and development of local overheating, the regions with $T > 200$ °C were tracked from 5 to 8.5 s, as shown in Figure 6.

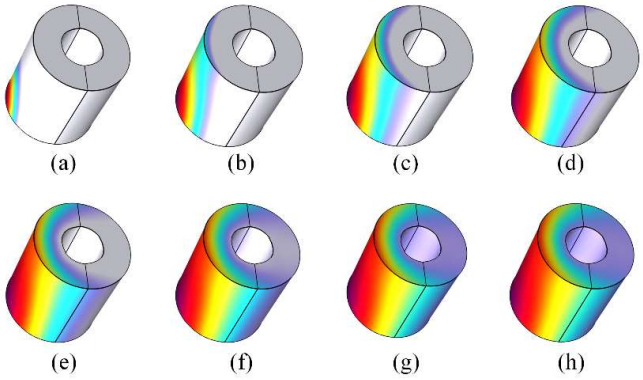

Figure 6. Over-temperature zone diagrams of glass-to-metal seal during laser welding. (**a**) $t = 5$ s; (**b**) $t = 5.5$ s; (**c**) $t = 6$ s; (**d**) $t = 6.5$ s; (**e**) $t = 7$ s; (**f**) $t = 7.5$ s; (**g**) $t = 8$ s; (**h**) $t = 8.5$ s.

At 5 s, only a very small over-temperature region appears on the weld-facing side of the seal. As the welding time increases to 5.5–6 s, this region expands within Zone 1 and subsequently spreads rapidly toward the remaining part of the seal. By 8–8.5 s, most or nearly all of the seal exceeds the 200 °C temperature tolerance.

Therefore, the welding duration was limited to 5 s. Under this condition, the over-temperature region remains confined to a small localized area, thereby minimizing the risk of thermal damage to the glass-to-metal seal. This process setting is expected to prevent sealing failure and preserve the hermeticity of the HRG. For practical implementation of the optimized 5 s welding duration, the laser scanning angular velocity was increased accordingly to complete the entire circumferential weld within 5 s, with a slight overlap to ensure seam continuity. The faster scanning speed reduces the local heating duration and promotes a more uniform heat distribution, thereby limiting localized heat accumulation and reducing the risk of overheating at the glass-to-metal seals.

5. Structure Optimization of the Gyroscope

The preceding sections optimized the getter activation and cover-plate welding conditions by controlling the thermal loads introduced during packaging. However, the resulting temperature field is determined not only by the heat-source conditions but also by the intrinsic heat-transfer characteristics of the HRG structure. In particular, the housing material and the geometric dimensions of the main heat-transfer paths directly affect heat propagation from the getter to the resonator and glass-to-metal seals. Therefore, the housing material and key structural dimensions were further investigated to reduce the thermal response of temperature-sensitive components and improve the overall thermal stability of the HRG.

5.1. Effect of Material Properties

The housing material plays an important role in determining heat propagation within the HRG package. In the original design, 4J36 alloy is used because of its favorable sealing and manufacturing properties. However, from the perspective of thermal management, it remains necessary to determine whether 4J36 provides the most suitable temperature response during getter activation. In addition to thermal performance, candidate housing materials should satisfy the basic requirements of weldability, corrosion resistance, mechanical strength, and manufacturing compatibility. Accordingly, 4J36, 4J29, 4J32, and 3J53 alloys were selected for comparison.

To isolate the influence of housing material, the remaining model parameters were kept unchanged, and a material sweep was performed in COMSOL. Figure 7 compares the three-dimensional temperature fields of the glass-to-metal seals and resonator for the four candidate alloys at $t = 10$ min of getter activation.

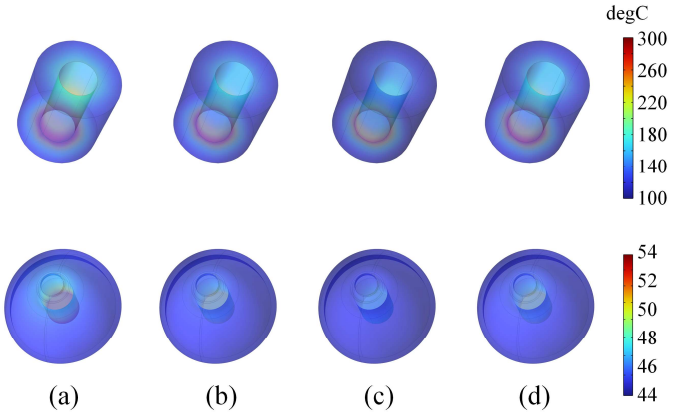

Figure 7. 3D temperature field diagrams of glass-to-metal seal and resonator under different alloy materials. (**a**) 4J36; (**b**) 4J29; (**c**) 4J32; (**d**) 3J53.

As shown in Figure 7, the housing material noticeably affects both the overall temperature level and the spatial temperature distribution of the HRG. Among the four candidate materials, the 4J32 case exhibits the lowest overall resonator temperature and the most uniform temperature distribution, whereas more pronounced temperature gradients are observed for the other materials. These results suggest that 4J32 can more effectively limit the thermal influence of getter activation on the resonator.

To quantitatively evaluate the material-dependent thermal response of the resonator, minimum temperature, maximum temperature, average temperature, and temperature range over the resonator surface are summarized in Table 1.

Table 1. Surface temperatures of resonators for various alloy materials.

Material	Minimum Temperature, °C	Maximum Temperature, °C	Average Temperature, °C	Range, °C
4J36	51.53	58.57	51.95	7.04
4J29	50.48	57.13	50.97	6.65
4J32	50.06	56.17	50.43	6.11
3J53	50.92	58.27	51.34	7.35

As summarized in Table 1, 4J32 exhibits the lowest minimum, maximum, and average resonator temperatures, with values of 50.06, 56.17, and 50.43 °C, respectively. It also produces the smallest temperature range of 6.11 °C among the four candidate materials. Compared with the original 4J36 housing, the use of 4J32 reduces the average resonator temperature from 51.95 to 50.43 °C and the maximum temperature from 58.57 to 56.17 °C. More importantly, the temperature range decreases from 7.04 to 6.11 °C, corresponding to a reduction of approximately 13.2%, indicating improved temperature uniformity across the resonator. Although the reduction in the absolute temperature level is moderate, the consistently lower temperature indices and smaller temperature range demonstrate that 4J32 provides the most favorable thermal response among the investigated alloys. Therefore, considering both thermal performance and engineering feasibility, 4J32 was selected as the housing material for the optimized HRG.

5.2. Effect of Structural Sizes

After selecting the housing material, the geometric parameters governing the principal heat-transfer paths were further optimized. Two dimensions were considered: the housing wall length, which determines the thermal coupling between the getter and the resonator, and the pin length, which governs conductive heat transfer from the getter to the glass-to-metal seals. Their effects on the corresponding temperature-sensitive components are summarized in Figure 8.

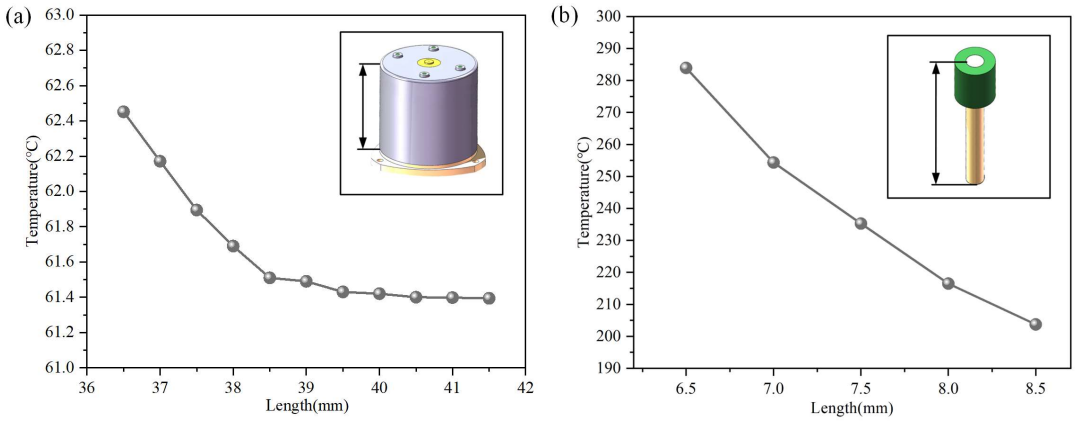

Figure 8. Effects of structural dimensions on the thermal response: (**a**) housing wall length versus average resonator surface temperature; (**b**) pin length versus maximum glass-to-metal-seal temperature.

The initial housing wall length in the original HRG design was 37 mm. The housing wall length directly determines the separation between the getter and the resonator and may therefore affect the thermal coupling between them. To evaluate this effect, the housing wall length was varied, and the average resonator surface temperature at the end of the 20 min dual-getter activation process was recorded, as shown in Figure 8a. Unlike the material comparison in Figure 7, where $t = 10$ min was selected as a representative transient time point to compare the relative temperature-field characteristics of different housing materials under identical heating conditions, the present analysis focuses on the thermal response accumulated over a complete getter activation cycle. Therefore, $t = 20$ min was selected as the evaluation time for structural-dimension optimization. The different evaluation times also account for the difference in resonator temperature levels between Figures 7 and 8 and should not be interpreted as a direct quantitative comparison between the two analyses.

As shown in Figure 8a, the average resonator temperature decreases as the housing wall length increases. However, the magnitude of the reduction becomes progressively smaller when the wall length exceeds approximately 38.5 mm. Further increasing the wall length would therefore provide only limited additional thermal benefit while increasing the package size, mass, and manufacturing complexity. Accordingly, a housing wall length of 38.5 mm was selected as a compromise between thermal performance and structural constraints.

In addition to the resonator, the glass-to-metal seals are also affected by heat transferred through the pins connected to the getter. The initial pin length in the original HRG design was 7 mm. To investigate the influence of this geometric parameter, the pin length was varied from 6.5 to 8.5 mm, and the corresponding maximum glass-to-metal-seal temperature was calculated, as shown in Figure 8b. The simulation results show that the maximum seal temperature decreases monotonically with increasing pin length. This trend is consistent with the expectation that increasing the heat-transfer distance along the pins may weaken conductive heat transfer from the getter to the nearby seals. Within the investigated range, a pin length of 8.5 mm produced the lowest maximum seal temperature. Considering the

package-size and lightweight-design constraints, 8.5 mm was therefore selected for the optimized structure.

Taken together, the material and dimensional analyses establish the thermally optimized HRG structure. The housing material was changed from 4J36 to 4J32, while the housing wall length and pin length were set to 38.5 and 8.5 mm, respectively. These structural modifications complement the process optimization described in the preceding sections by reducing the simulated thermal response of the resonator and glass-to-metal seals.

6. Experimental Validation

Based on the preceding simulation analyses, an optimized HRG packaging scheme was established, including a 4J32 Kovar housing, a housing wall length of 38.5 mm, a pin length of 8.5 mm, a cover-plate laser welding duration of 5 s, and dual-getter activation at 800 °C for 20 min. To evaluate the engineering applicability of this simulation-guided optimization, HRG prototypes were fabricated using these optimized structural and process parameters. The experimental validation was organized into four parts: implementation of the optimized packaging process, comparison of single- and dual-getter activation strategies, evaluation of package hermeticity after completion of the high-temperature packaging process, and characterization of dynamic-parameter stability throughout the major manufacturing stages.

6.1. Experimental Implementation of the Optimized Packaging Process

The experimental packaging procedure is illustrated in Figure 9. After precision assembly of the HRG components, the cover plate was hermetically sealed using the optimized laser welding condition. Preliminary vacuum pumping was subsequently performed to reduce the internal gas pressure, followed by electrical activation of the getters.

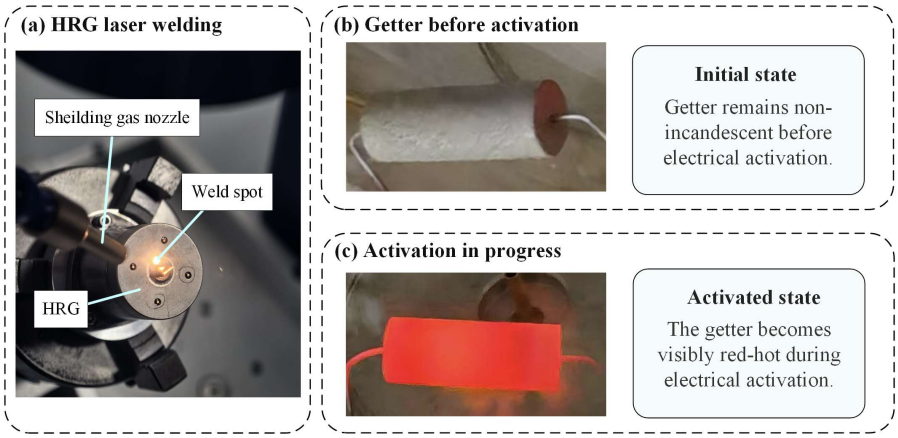

Figure 9. Experimental packaging process: (**a**) representative illustration of HRG cover plate laser welding; (**b**) getter before activation; (**c**) getter during electrical activation.

As shown in Figure 9a, laser welding was used to complete the hermetic sealing of the cover plate. Because the dedicated fixture used in the actual packaging process obstructed the welding region and was not suitable for clear photographic documentation, Figure 9a is presented as a representative illustration of the laser welding operation rather than the actual fixture configuration. The HRG prototypes were nevertheless welded using the actual packaging fixture and the optimized welding parameters. Figures 9b and 9c show representative photographs of the getter before and during electrical activation, respectively. Because the getter is located inside the package and cannot be directly observed after final packaging, these photographs are provided to illustrate its activation state. Before activation, the getter exhibits a brownish-gray appearance, whereas it becomes visibly crimson red

during electrical heating. The activation condition was maintained at 800 °C for 20 min in accordance with the optimized process parameters.

After implementation of the optimized packaging process, the experimental validation first focused on the influence of the getter activation strategy on the dynamic characteristics of the HRG.

6.2. Experimental Comparison of Getter Activation Strategies

The simulations in Section 3 showed that simultaneous dual-getter activation provides a more symmetric resonator temperature field than single-getter activation. To experimentally assess whether this difference is reflected in the dynamic parameters of the HRG, a controlled comparison between single-getter and dual-getter activation was performed while the remaining process conditions were kept unchanged. For each gyroscope, the relevant dynamic parameters were measured before and after getter activation. $Q_{\max}$ and $Q_{\min}$ denote the maximum and minimum Q factors, respectively, and ΔQ was calculated as follows:

$$\Delta Q = \frac{2|Q_{max} - Q_{min}|}{Q_{max} + Q_{min}} \times 100\% \quad (7)$$

Using Equation (7), ΔQ was calculated for each gyroscope before and after getter activation. To quantify the magnitude of the activation-induced variation, the relative change rates of Δf and ΔQ were calculated as the absolute difference between the values before and after activation normalized by the corresponding pre-activation value, and were expressed as percentages. The measured parameters and their relative changes for the single-getter and dual-getter activation cases are summarized in Table 2.

Table 2. Performance comparison of HRGs under different getter activation methods.

Activation Method	Gyroscopes	State	Δf, mHz	Δf Change Rate	$Q_{\max}$ ($\times 10^4$)	$Q_{\min}$ ($\times 10^4$)	ΔQ	ΔQ Change Rate
Single Getter	#1	Before	1.53	11.11%	1281.67	1174.59	8.72%	31.19%
		After	1.36		1350.11	1271.50	6.00%	
	#2	Before	1.20	15.00%	960.33	897.91	6.72%	49.55%
		After	1.38		965.45	933.28	3.39%	
Dual Getter	#3	Before	0.93	3.23%	1630.00	1607.00	1.42%	2.82%
		After	0.96		1679.00	1656.00	1.38%	
	#4	Before	1.13	4.42%	872.84	833.37	4.63%	5.83%
		After	1.08		1087.64	1035.58	4.90%	

The Q factors in Tables 2–4 were obtained by the electrical ring-down measurement method. The resonator was electrostatically excited to a stable standing-wave vibration. After disabling amplitude control, its electrically detected vibration-amplitude envelope was fitted by $A(t) = A_0 \exp(-t/\tau_A)$. The Q factor was calculated as $Q = \pi f_0 \tau_A$, where f_0 is the resonant frequency and τ_A is the amplitude-decay time constant [22,23]. The standing-wave orientation was held fixed during each decay measurement.

It should first be noted that the four HRGs exhibit different initial dynamic parameters because of device-to-device variations. Therefore, a direct comparison of the absolute values of Δf, $Q_{\max}$, $Q_{\min}$, and ΔQ among different gyroscopes is not appropriate. Instead, the analysis focuses on the changes in these parameters before and after getter activation for each individual device, thereby evaluating the disturbance introduced by the high-temperature activation process.

Table 3. Dynamic parameters and relative changes in HRGs under the original packaging process.

Process Stage	Gyroscope	Frequency, Hz	Δf, mHz	Δf Change Rate	Q_{max} ($\times 10^4$)	Q_{min} ($\times 10^4$)	ΔQ	ΔQ Change Rate
Assembly	#1	7206.91	0.89	/	1677.12	1534.99	8.85%	/
	#2	7206.23	0.95	/	1305.60	1097.92	17.28%	/
	#3	6933.16	0.83	/	1579.49	1523.16	3.63%	/
Welding	#1	7204.51	0.94	5.62%	1753.19	1422.60	20.82%	135.25%
	#2	7206.58	2.19	130.53%	1744.23	1532.85	12.90%	25.35%
	#3	6931.19	1.20	44.58%	1634.76	1599.92	2.15%	40.77%
Getter Activation	#1	7203.95	2.18	131.91%	1757.13	1251.76	33.59%	61.34%
	#2	7205.20	2.21	0.91%	1558.94	1147.86	30.37%	135.43%
	#3	6931.11	2.62	118.33%	1686.16	1183.41	35.04%	1529.77%

Table 4. Dynamic parameters and relative changes in HRGs under the optimized packaging process.

Process Stage	Gyroscope	Frequency, Hz	Δf, mHz	Δf Change Rate	Q_{max} ($\times 10^4$)	Q_{min} ($\times 10^4$)	ΔQ	ΔQ Change Rate
Assembly	#1	7107.44	0.56	/	1462.00	1412.00	3.48%	/
	#2	6384.68	0.89	/	1750.00	1687.00	3.67%	/
	#3	6913.40	0.99	/	1635.00	1609.00	1.60%	/
Welding	#1	7107.02	0.59	5.36%	1470.00	1417.00	3.67%	5.46%
	#2	6389.21	0.89	0.00%	1775.00	1720.00	3.15%	14.17%
	#3	6913.91	0.93	6.06%	1630.00	1607.00	1.42%	11.25%
Getter Activation	#1	7107.78	0.61	3.39%	1484.00	1433.00	3.50%	4.63%
	#2	6385.20	0.91	2.25%	1732.00	1673.00	3.47%	10.16%
	#3	6913.72	0.96	3.23%	1679.00	1656.00	1.38%	2.82%

As shown in Table 2, the HRGs subjected to single-getter activation exhibit Δf change rates of 11.11% and 15.00%, whereas the corresponding values for dual-getter activation are only 3.23% and 4.42%. A similar difference is observed for ΔQ. For the single-getter cases, ΔQ changes from 8.72% to 6.00% and from 6.72% to 3.39%, corresponding to relative changes of 31.19% and 49.55%, respectively. In contrast, the dual-getter cases show much smaller variations, from 1.42% to 1.38% and from 4.63% to 4.90%, with relative changes of only 2.82% and 5.83%.

Although the direction of the parameter variation is not identical for all devices, the magnitudes of both Δf and ΔQ changes are consistently smaller for the dual-getter cases under the investigated conditions. This indicates that simultaneous dual-getter activation introduces a smaller disturbance to the key dynamic parameters of the HRG during the high-temperature activation process. Therefore, compared with sequential single-getter activation, simultaneous dual-getter activation is more favorable for maintaining dynamic parameter stability during packaging. This experimental trend is also consistent with the more symmetric resonator temperature field predicted in Section 3, and simultaneous dual-getter activation was consequently adopted in the optimized packaging process.

6.3. Hermeticity Validation After High-Temperature Packaging

After selecting simultaneous dual-getter activation, the hermeticity of the HRG was evaluated after completion of the entire optimized packaging process. This verification is

particularly important because both major high-temperature steps may threaten package integrity through different thermal paths. During cover-plate welding, heat propagates from the annular weld toward the peripheral glass-to-metal seals, whereas during getter activation, localized heating may occur around the pin–seal regions. Consequently, the final hermeticity test was used to determine whether the combined thermal exposure associated with welding and getter activation resulted in detectable sealing failure.

Three HRG prototypes from the same production batch were tested after the optimized 5 s cover-plate welding and dual-getter activation process. A helium mass-spectrometer leak detector was employed using the spray-helium method. Helium was applied to the cover-plate welding region and the glass-to-metal seals, which represent the principal sealing structures exposed to thermal loading during the packaging process. The experimental configuration and a representative real-time leak-rate signal are shown in Figure 10.

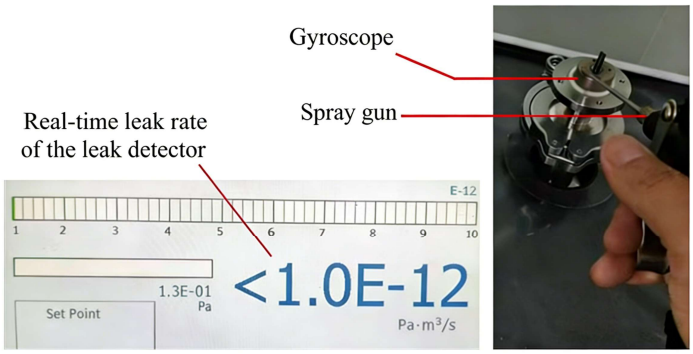

Figure 10. Schematic diagram of the inspection process.

The hermeticity of the packaged HRG was evaluated using an Agilent HLD PD03 (Agilent Technologies (China) Co., Ltd., Beijing, China) portable dry helium leak detector. As shown in Figure 10, the measured leak rate remained below 1×10^{-12} Pa·m^3/s. This leak-rate level has reached the lower detection range of current mainstream commercial helium mass spectrometer leak detectors, indicating that no detectable leakage occurred within the measurement capability of the instrument.

Figure 10 provides a representative leak-detection response for a single device. To further evaluate the repeatability of the hermetic performance and examine whether prolonged helium exposure produced any detectable leakage response, three HRGs were tested at helium spraying times of 10, 30, and 60 s. For all three HRGs, the indicated leak rates remained below 1×10^{-12} Pa·m^3/s at all three spraying times.

These results demonstrate the excellent hermeticity of the optimized HRG after packaging. The detector has a nominal minimum detectable rate of 5×10^{-13} Pa·m^3/s, but the effective reporting threshold used here was 1×10^{-12} Pa·m^3/s because lower settings yielded unstable readings. The results should therefore be interpreted as below this threshold, not as an exact leak-rate value.

6.4. Dynamic-Parameter Stability During Packaging

Although the helium leak tests verify the integrity of the sealing structure, satisfactory hermeticity alone does not demonstrate that the high-temperature packaging processes have negligible influence on HRG performance. Thermal loading during laser welding and getter activation may also alter the dynamic state of the resonator. Therefore, the key dynamic parameters were further measured at successive manufacturing stages to evaluate the influence of the two high-temperature packaging steps. The measured Q factor reflects combined energy losses, including gas, thermoelastic, and support-related contributions [12,21].

To provide a direct reference for evaluating the effectiveness of the proposed optimization, three HRGs fabricated using the original packaging process were first characterized at three successive stages: after assembly, after cover-plate welding, and after getter activation. The resonant frequency, frequency split Δf, Q_{max}, Q_{min}, and ΔQ were measured at each stage. The relative changes in Δf and ΔQ at each packaging stage were calculated with respect to the immediately preceding stage. The results are summarized in Table 3.

As shown in Table 3, the original packaging process produces substantial and device-dependent variations in the key dynamic parameters, while the resonant frequency remains comparatively stable. During cover-plate welding, the Δf change rates are 5.62%, 130.53%, and 44.58%, and the corresponding ΔQ change rates are 135.25%, 25.35%, and 40.77%, respectively. During getter activation, the corresponding change rates are 131.91%, 0.91%, and 118.33% for Δf and 61.34%, 135.43%, and 1529.77% for ΔQ. The exceptionally large relative change for HRG #3 reflects an increase in ΔQ from 2.15% to 35.04%. After packaging, all three original HRGs exhibit Δf values of 2.18–2.62 mHz and ΔQ values of 30.37–35.04%, demonstrating considerable disturbance to the resonator dynamic state and marked degradation of Q factor uniformity.

These results provide a direct experimental basis for assessing the effectiveness of the simulation-guided optimization. Accordingly, HRGs incorporating the optimized housing material, structural dimensions, welding condition, and simultaneous dual-getter activation strategy were subsequently characterized using the same stage-by-stage procedure. The corresponding results are presented in Table 4.

Table 4 summarizes the dynamic parameters of the HRGs fabricated using the optimized packaging process. In contrast to the pronounced variations observed under the original process, the optimized HRGs exhibit much smaller stage-to-stage changes in both Δf and ΔQ. During cover-plate welding, the Δf change rates do not exceed 6.06%, while the corresponding ΔQ change rates do not exceed 14.17%. During getter activation, the maximum changes in Δf and ΔQ are only 3.39% and 10.16%, respectively. The resonant frequencies also remained stable throughout the three manufacturing stages, with relative variations below 0.08%.

More importantly, Δf remains below 1 mHz for all three optimized HRGs, and ΔQ remains within 1.38–3.67% throughout the packaging process. After completion of getter activation, the final ΔQ values are 3.50%, 3.47%, and 1.38%, respectively, with no systematic increase relative to the assembly state. Compared with the much larger parameter variations observed under the original packaging process, these results indicate that the optimized material, structural dimensions, welding condition, and dual-getter activation strategy substantially improve the stability of the key dynamic parameters during high-temperature packaging. Furthermore, the Q factors of the gyroscopes after activation all exceeded 14 million.

Overall, the comparison between the original and optimized packaging processes provides direct experimental evidence that the simulation-guided optimization effectively limits packaging-induced variations in the key dynamic parameters of the HRG. Here, the temperature distributions are simulation predictions, while the changes in Δf and ΔQ and the leak test responses are experimentally measured. Since several modifications were implemented together, the experiments support the combined process improvement rather than a separate numerical contribution for each modification.

7. Conclusions

The localized thermal loads produced by getter activation and cover-plate laser welding were analyzed for an HRG vacuum package. A coupled thermal model was used to identify the dominant heat-transfer paths and the locations most susceptible to overheating. The

model was then used to optimize the activation strategy, welding duration, housing material, and key structural dimensions.

The main findings are as follows: (1) Simultaneous dual-getter activation substantially improves resonator thermal symmetry, while the peak average seal temperature remains 169.2 °C and the local $T > 200$ °C region remains small after cooling. (2) During cover-plate welding, the seal half facing the annular weld heats fastest. Limiting the welding duration to 5 s keeps the over-temperature region localized. (3) A 4J32 housing, a 38.5 mm housing wall length, and an 8.5 mm pin length provide the best thermal compromise within the investigated design range.

Experimental validation further confirmed the effectiveness of the optimized scheme. Compared with the pronounced stage-to-stage variations observed under the original packaging process, the optimized HRGs exhibited substantially smaller changes in Δf and ΔQ during both welding and getter activation. The leak rate of all tested HRGs remained below 1×10^{-12} Pa·m^3/s. Across assembly, welding, and getter activation, Δf remained below 1 mHz and ΔQ remained between 1.38% and 3.67%, with a maximum measured Q factor of 1.775×10^7. These results indicate that the optimized high-temperature packaging process effectively maintained the key dynamic parameters stable while preserving package hermeticity.

This work establishes a systematic thermal optimization framework for HRG vacuum packaging by integrating packaging-process control, material selection, and structural parameter optimization. The optimized packaging process provides high-level gyroscope dynamic parameters for further development of high-performance HRGs.

Future work will focus on developing a fully coupled thermo-mechanical model to quantitatively evaluate the residual stress distribution throughout the entire HRG structure during high-temperature packaging, thereby further clarifying the relationship between packaging-induced thermal loads, structural response, and dynamic-parameter stability.

Author Contributions: M.K.: writing—original draft, writing—review and editing, visualization, software, data curation. Y.P.: project administration, conceptualization, resources. Y.L.: writing—review and editing, methodology, funding acquisition, resources, formal analysis. K.Y.: investigation, validation. Y.J.: investigation, resources. H.L.: project administration, resources, supervision. J.S.: validation, investigation. S.Z.: software, validation. X.J.: writing—review and editing, supervision. All authors have read and agreed to the published version of the manuscript.

Funding: This work was supported in part by the science and technology innovation Program of Hunan Province (Grant No. 2026RC3119), and in part by the "Young Talents" high-level training program of the National University of Defense Technology.

Institutional Review Board Statement: Not applicable.

Informed Consent Statement: Not applicable.

Data Availability Statement: The original contributions presented in this study are included in the article. Further inquiries can be directed to the corresponding authors.

Conflicts of Interest: The authors declare no conflicts of interest.

References

1. Maslov, A.A.; Maslov, D.A.; Ninalalov, I.G.; Merkuryev, I.V. Hemispherical resonator gyros (an overview of publications). *Gyrosc. Navig.* **2023**, *14*, 1–13. [CrossRef]
2. Wang, F.; Wang, J.; Yi, Z.; Ye, C.; Zhu, Y. Application of conductive graphene films for high-performance hemispherical resonator gyroscopes. *Appl. Phys. Lett.* **2024**, *125*, 174102. [CrossRef]
3. Guo, K.; Wu, Y.; Zhang, Y.; Xiao, D.; Wu, X. Adaptive compensation of damping asymmetry in whole-angle hemispherical resonator gyroscope. *AIP Adv.* **2020**, *10*, 105109. [CrossRef]

4. Yao, X.; Zhao, H.; Su, Z.; Gu, X.; Chu, S. A study of the effect of temperature on the capacitance characteristics of a metal-μ hemisphere resonant gyroscope. *Sensors* **2024**, *24*, 7088. [CrossRef]
5. Zhou, X.; Wen, J.; Han, S.; Li, C. Compensation of temperature-induced bias drift in hemispherical resonator gyroscopes: An inherent data-driven architecture. *Micromachines* **2025**, *16*, 357. [CrossRef]
6. Wang, X.; Wu, W.; Fang, Z.; Luo, B.; Li, Y.; Jiang, Q. Temperature drift compensation for hemispherical resonator gyro based on natural frequency. *Sensors* **2012**, *12*, 6434–6446. [CrossRef]
7. Deng, K.; Zeng, L.; Pan, Y.; Jia, Y.; Luo, Y.; Tao, Y.; Yuan, J. Frequency mismatch analysis of hemispherical shell resonators with both radius and thickness imperfections. *J. Appl. Phys.* **2024**, *135*, 194501. [CrossRef]
8. Wang, Y.; Pan, Y.; Qu, T.; Jia, Y.; Yang, K.; Luo, H. Decreasing frequency splits of hemispherical resonators by chemical etching. *Sensors* **2018**, *18*, 3772. [CrossRef]
9. Zhao, W.; Rong, Y.; Li, C.; Wang, Y.; Cai, X.; Yu, X. High precision hemispherical resonator gyroscopes with oven control systems. *IEEE Sens. J.* **2021**, *21*, 7388–7401. [CrossRef]
10. Zeng, L.; Deng, K.; Pan, Y.; Li, J.; Tang, X.; Luo, H. Self-calibration of hemispherical resonator gyroscopes under drastic changes of ambient temperature based on mode reversal. *Sens. Actuators A Phys.* **2024**, *366*, 114986. [CrossRef]
11. Xu, Z.; Yi, G.; Zhu, W. An accurate thermoelastic model and thermal output error analysis of a hemispherical resonator gyroscope under varying temperatures. *Mech. Syst. Signal Process.* **2022**, *170*, 108760. [CrossRef]
12. Yuan, L.; Wang, N.; Xie, R.; Wei, Z.; Zeng, Q.; Wang, C. Study on the mechanism of energy dissipation in hemispherical resonator gyroscope. *Sensors* **2025**, *25*, 74. [CrossRef]
13. Mittapally, G.K.M.; Dantala, D.; Chhabra, I.M.; Pasalapudi, N.V.N.R.; Das, K.C. Influence of vacuum and its degradation on the sensing element of the Coriolis vibratory gyroscope. *J. Vibroeng.* **2021**, *23*, 1716–1726. [CrossRef]
14. Ramachandran, A.V.; Zorzano, M.; Martín-Torres, J. Numerical heat transfer study of a space environmental testing facility using COMSOL Multiphysics. *Therm. Sci. Eng. Prog.* **2022**, *29*, 101205. [CrossRef]
15. Sartori, E.; Siragusa, M.; Sonato, P.; Siviero, F.; Mura, M.; Maccallini, E.; Ferrara, A.; Manini, P.; Hanke, S.; Day, C. Development of non-evaporable getter pumps for large hydrogen throughput and capacity in high vacuum regimes. *Vacuum* **2023**, *214*, 112198. [CrossRef]
16. Wang, L.; Li, Y.; Guo, D.; Jin, Q.; Zhang, Z.; Yang, Z. Effect of adding Al on the phase structure and gettering performance of TiZrV non-evaporable getter materials. *Materials* **2024**, *17*, 1969. [CrossRef]
17. Shi, Q.; Wang, S.; Wang, P.; Ma, Y.; Tan, B.; Shi, S.; Huang, T.; Sun, F.; Wang, L.; Zhao, X.; et al. Effect of atomic-scale microstructures on TiZrV non-evaporable getter film activation. *J. Vac. Sci. Technol. B* **2023**, *41*, 064202. [CrossRef]
18. Shi, Q.; Wang, S.; Ma, Y.; Shi, S.; Sun, F.; Wang, P.; Huang, T.; Wang, L.; Zhao, X.; Lu, M.; et al. Cage effect of film mesoscopic structure on activation of TiZrHfV non-evaporable getter. *Vacuum* **2024**, *222*, 113051. [CrossRef]
19. Bourim, E.; Kim, H.Y.; Chung, N. Development and characterization of non-evaporable getter thin films with Ru seeding layer for MEMS applications. *Micromachines* **2018**, *9*, 490. [CrossRef]
20. Zheng, K.; Wang, T.; Wu, M.; Gu, D.; Lv, W.; Wang, L. Research on performance of porous scaffold-based getter activated by induction heating and its application in MEMS device. *Vacuum* **2024**, *230*, 113626. [CrossRef]
21. Zeng, L.; Luo, Y.; Pan, Y.; Jia, Y.; Liu, J.; Tan, Z.; Yang, K.; Luo, H. A 5.86 million quality factor cylindrical resonator with improved structural design based on thermoelastic dissipation analysis. *Sensors* **2020**, *20*, 6003. [CrossRef]
22. Lee, J.; Yun, S.W.; Rhim, J. Design and verification of a digital controller for a 2-piece hemispherical resonator gyroscope. *Sensors* **2016**, *16*, 555. [CrossRef]
23. Ning, Y.; Wang, C.; Xi, B.; Tian, Z.; Zhang, B. Identification and correction of phase delay errors for hemispherical resonator gyroscopes. *Sci. Rep.* **2025**, *15*, 2078. [CrossRef]

Disclaimer/Publisher's Note: The statements, opinions and data contained in all publications are solely those of the individual author(s) and contributor(s) and not of MDPI and/or the editor(s). MDPI and/or the editor(s) disclaim responsibility for any injury to people or property resulting from any ideas, methods, instructions or products referred to in the content.